

On the coupling of CFD and CSD methodologies for modeling blast-structure interactions

J. D. Baum¹, E. L. Mestreau¹, H. Luo¹, R. Löhner², D. Pelessone³,
M. E. Giltrud⁴ & J. K. Gran⁵

¹*Center for Applied Computational Sciences, SAIC, USA*

²*CSI, George Mason University, USA*

³*Engineering and Software System Solutions, USA*

⁴*TDSH, Defense Threat Reduction Agency, USA*

⁵*Poulter Laboratory, SRI International, USA*

Abstract

This paper describes applications of a coupled Computational Fluid Dynamics (CFD) and Computational Structural Dynamics (CSD) methodology to the simulation of blast waves generated by bare explosive charges in a test facility with rigid and deformable walls. The coupled algorithm combines FEFLO98 (CFD) and MARS3D (CSD) via an embedded approach, where the CSD objects float through the CFD domain. This combination enables an easier and more accurate prediction of structural deformation, cracking and failure under blast loading.

Several experiments were conducted to characterize blast load and structural response as a function of charge size, weapon ignition point (nose or tail) and orientation (horizontal or vertical). The numerical simulations helped in understanding the experimental results, some of which were not intuitively understood. Good agreement between the experimental results and the numerical predictions were demonstrated for pressure data, blast loading and the corresponding structural response.

Keywords: blast-structure interaction, coupled CFD and CSD, blast wave evolution, structural response to blast loading.



1 Introduction

The objective of this study is to validate and apply the coupled CFD/CSD methodology to the simulation of bare/cased weapons detonation/fragmentation, and blast and fragment interactions with rigid and deformable structures. These applications constitute a very severe test to the numerical methodology as they require modeling of several complex and interacting physical phenomena: a) Detonation wave initiation and propagation; b) CSD modeling of case expansion and fragmentation; c) Blast wave expansion through the breaking case, and around the flying fragments; and e) Fragments and airblast impact on the structure and the resulting structural deformation. To model the physics involved, elasto-plastic material models with rupture criteria (CSD) are required, coupled with either the Euler or the Reynolds-Averaged Navier-Stokes (CFD).

Two approaches can be used to model fluid/structure interaction. The ‘tight coupling’ approach requires solving both CFD and CSD as one coupled set of equations with the drawback of requiring the complete rewrite of both solvers. The second approach, called ‘loose coupling’, decouples the CFD and CSD sets of equations and uses projection methods to transfer interface information between the CFD and CSD domains. By building on pre-existing and well-established codes, a loose-coupled solver can be assembled with minimum modifications to either of the two solvers. This is the chosen approach. The modularity is kept by the addition of a “controller” code, which handles the transfer of information between the different solvers [1]. This module handles non-matching meshes at the interface and incorporates conservative interpolation schemes and fast techniques for neighbor search. The correspondence between fluid and structure points is automatically deduced, without any user input. Time synchronization between the CFD and CSD solvers is also managed by the controller code, using a leap-frog approach.

The motion of a solid or a deforming body through the fluid domain can be modeled using two approaches: the glued approach and the embedded approach. The glued approach requires the use of expensive automatic remeshing routines, and is prone to failure due to structure mesh penetration highly deformed elements. In the second approach, the embedded CSD mesh floats through the CFD domain without body/surface conformance. The faster Eulerian formulation (rather than the slower ALE) is used. The only extra intensive steps involve the identification of the crossed edges and proper modeling of the boundary conditions. On the negative side, this method requires the use of new more complex boundary conditions of first and maybe second order.

Over the past several years, we have developed and successfully applied the traditional glued approach [2,3]. However, this approach has failed for simulations involving singular points when the CSD contact algorithm can not prevent inter-penetrations and tiny gaps to form. Moreover, for applications such as crack propagation and cased weapons fragmentation, the superfine resolution required to properly model the flow within the cracks becomes prohibitive. Finally, the meshing procedure itself may fail due to high level of complexity of the topology. These shortcomings of the glued approach are, conversely, the



strengths of the embedded approach, where the bodies float through the CFD mesh. The closeness of bodies and possible penetration poses no difficulty to the CFD solution.

In the present study, we sought to validate the coupled CFD/CSD methodology against high-quality experimental data. While the geometry modeled is relatively simple, the physical processes modeled are complex. The first step of the validation study, describes in this paper, deals with modeling the detonation of bare charges placed in a tube, and the resulting airblast interaction with rigid as well as deformable walls. In future papers, we will describe the results obtained for cased weapons. In such case, the methodology must model the case fragmentation and the extra loads resulting from the fragment impacts.

2 Methodology

Any blast-structure simulation proceeds through the following stages: Pre-Processing, Grid Generation, Flow Solver, and Post-Processing. The pre-processor tool used is FECAD [4]. It acquires and sets-up geometric data, boundary conditions and desired mesh size for both CFD and CSD. The grid generation, which is based on an advancing front method, is then performed for both CFD and CSD using FRGEN3D [5]. The CFD mesh is composed of triangular (surface) and tetrahedral (volume) elements. The CSD mesh includes beams, triangular or quad shells and bricks for the solids. The quads shells are the result of aggregation of triangles while the bricks are the subdivision of tetrahedral elements followed by smoothing techniques.

The flow solver employed is FEFLO98, a 3-D adaptive, unstructured, edge-based hydro-solver based on the Finite-Element Method Flux-Corrected Transport (FEM-FCT) [6]. It solves the Arbitrary Lagrangean-Eulerian (ALE) formulation of the Euler and Reynolds-averaged turbulent, Navier-Stokes equations. The high order scheme used is the consistent-mass Taylor-Galerkin algorithm. Combined with a modified second-order Lapidus artificial viscosity scheme, the resulting scheme is second-order accurate in space, and fourth-order accurate in phase. The spatial mesh adaptation is based on local H-refinement, where the refinement/deletion criterion is a modified H2-seminorm [6] based on user-specified unknowns. For blast wave propagation, these typically are a blend of density and energy. FEFLO98 supports various equations-of-state including real air, water, SESAME and JWL with and without afterburning. Particles are also modelled, exchanging mass, momentum and energy with the fluid. Particles may burn, reducing their radius in time.

The structural dynamics solver used is MARS3D [7], a modern variant of DYNA3D [8]. Both codes are unstructured, explicit finite element codes, well suited for modeling large deformations. They provide a good base for non-linear materials with elasto-plastic comportemental laws with rupture. These codes incorporate a large library of materials and various equations-of-state, as well as many kinematic options, such as slidelines and contacts.



3 Results

3.1 The test matrix

The test facility developed by SRI [9] is shown schematically in Fig 1. The facility consists of a concrete pipe grouted inside a steel tube with a circular cross section truncated by a planar concrete floor. One end of the tube is open. The other end contains a partial steel bulkhead with either a well-instrumented steel plate containing 17 pressure gauges or a deformable set of end-plates. While the test matrix includes detonation of bare as well as cased charges, the discussion in this paper will only deal with the bare charges. These tests examine the effect of varying charge weight, charge orientation (vertical or horizontal) and ignition point (nose or tail), on the blast load and its impact on the closed end of the tube. The charges were either nose- or tail-detonated, oriented either vertically or horizontally.

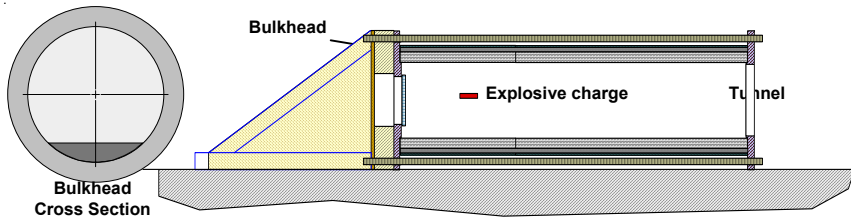


Figure 1: Schematics of the test facility.

The quality of measured data was excellent, which was one of the incentives for conducting this validation study. The use of Composition-B explosive was also a compelling factor as it eliminates many of the uncertainties associated with non-ideal explosive.

3.2 Bare charges against an instrumented rigid end-wall

Two cylindrical charge sizes were tested, composed of either 174grams or 263grams of Composition B-3. Both charges CG were placed at the identical location relative to the flat floor and the end wall. Both charges were axially placed in the direction of the tube axis, normal to the end panels (Fig 1).

The numerical simulations are conducted in two stages. In a first phase, a highly refined small region around the HE is modelled, allowing for a highly accurate simulation of the detonation and product expansion. This phase is terminated shortly after detonation completion. The flow field is then interpolated onto the domain that contains the complete tube. Both explosive charges have a medium L/D ratio, which contributes to the significant asymmetry of the detonation products expansion. The most noticeable is a strong jet propagating upstream of the nose-end. This behavior has been observed previously for medium and large L/D cylindrical explosives [10].

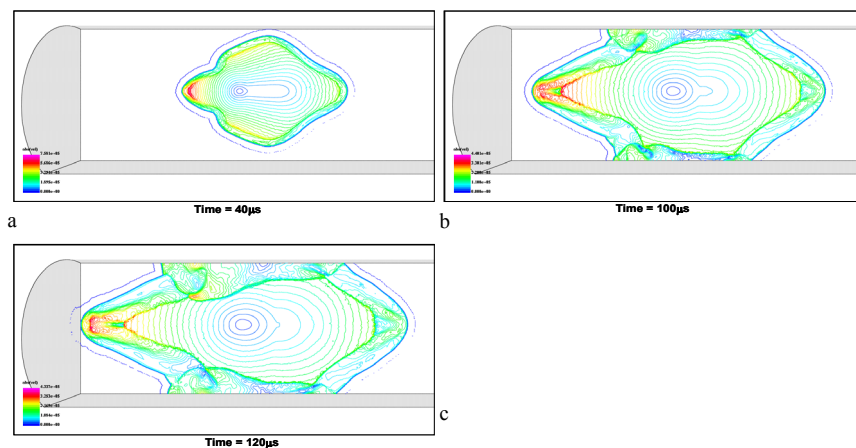


Figure 2: Velocity contours showing blast wave evolution and jet formation.

Figures 2a through 2c show the predicted velocity contours at times of $40\mu\text{s}$, $100\mu\text{s}$ and $120\mu\text{s}$, respectively. For clarity reason, results are shown only on the plane of symmetry for a small section of the tube. These results were obtained for the 174grams tail-detonated charge. Very similar results are observed for the 263grams bare charge. The formation of a strong jet off the nose-end is clearly visible. The pressure amplitude behind this jet is significant and fairly focused.

A sequence of pressure contours is shown in Figs 3a through 3f, for respectively $180\mu\text{s}$, $200\mu\text{s}$, $220\mu\text{s}$, $240\mu\text{s}$, $260\mu\text{s}$, and $280\mu\text{s}$. The sequence shows the incident blast wave impact on the wall. Notice: a) The high-amplitude reflected pressure zone (colored magenta) is limited to a small circle about the center of the jet impact (axis of the cylinder), as shown in Figs 3a through 3e. This high pressure is observed only at the narrow-diameter jet zone, where the high-velocity jet stagnates; b) The temporal evolution of the circumferential blast wave. This is the wave generated by the detonating cylinder at angles between 45° and 135° , and contains most of the detonation energy. This blast wave propagation is easily observed on top and bottom of the plane of symmetry, though it is circumferential. This wave impacts the end wall first at the center top (Fig 3d at $240\mu\text{s}$), expanding to the rest of the end-plate/tube corner and only then propagates towards the center (Fig. 3f); and c) While the narrow central jet has a high pressure, it carries significantly less energy than the slower, later-arriving circumferential blast wave that carries most of the energy. Nevertheless, it should be expected that the damage to the deformable steel panels will be initiated at the narrow jet-impact location, along the axis of the cylinder.

Fig. 4 shows the arrangement of the pressure transducers on the closed, rigid end wall of the tube. Comparison of predicted and measured pressure and impulse time histories, obtained for the tail-detonated 174grams cylindrical charge, is shown in Fig. 5a through 5e. These figures present in geometric order the results at all stations from just below the explosive axis. The vertical distance between stations is 1.508 inches. The initial jet peak pressure, impacting at about

125 μ s, reduces from station 2 through 14 (in brackets), from about 10,000psi [2] \rightarrow 4,400psi [1] \rightarrow 500psi [3] \rightarrow 400psi [9] \rightarrow 300psi [14]. Peak pressure for the main blast, the one that initially expanded circumferentially, increases from the circumference to the center, from 1,900psi [14] \rightarrow 2,500psi [9] \rightarrow 3,000psi [3] \rightarrow 3,200psi [1] \rightarrow 3800psi [2]. The arrival time of this blast wave is about 250 μ s [14] \rightarrow 260 μ s [9] \rightarrow 270 μ s [3] \rightarrow 280 μ s [1] \rightarrow 290 μ s [2]. Finally, maximum impulse values (at 3.0ms) vary from 0.47psi-sec [14] \rightarrow 0.46psi-sec [9] \rightarrow 0.49psi-sec [3] \rightarrow 0.645psi-sec [1] \rightarrow 0.83psi-sec [2].

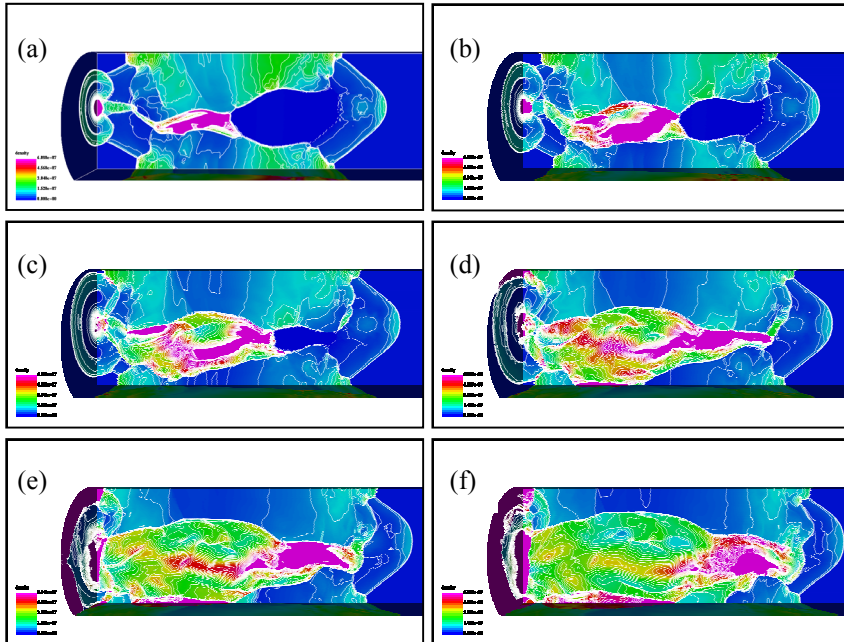


Figure 3: Pressure contours showing blast wave evolution. (a) Time = 180 μ s, (b) time = 200 μ s, (c) time = 220 μ s, (d) time = 240 μ s, (e) time = 260 μ s, (f) time = 280 μ s.

Finally, analysis of the maximum pressures and impulses observed at every point on the tube surfaces (perimeter, end wall and floor), over the duration of the simulation, highlighted two major processes discussed above: a) Blast (jet) wave focusing on the end wall with a very high pressure loading on a small diameter circle centered at impact point, and exponentially-decaying pressure amplitude outside this zone. Again, impact point is not at the center of the tube but on the axis of the charge; and b) High-impulse circular domain about the same point. High impulse zones are also observed at the stagnation and near-stagnation wall-tube intersection arcs. Similar results, qualitatively, were obtained for the 263 grams charge. The CG of this charge was placed at the same location, and this charge was also tail detonated. Finally, the same size charge was also nose-detonated. Here we observe that: 1) On the nose-end we do not

observe jet formation; and 2) It was expected to obtain higher impulse loads on the closed end from the closer nose-detonation than from the tail-detonated charge. However, the results are mixed due to the large loads exerted by the central jet. Near the jet impact point, the tail-detonated charge has a higher impulse than the nose-detonated charge. As the distance increases from impact point (cylinder axis), the two equilibrate. Further away, closer to the tube walls, the nose detonated charge imposes higher impulse loads.

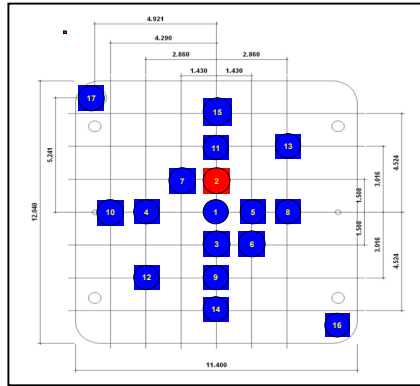


Figure 4: Transducer locations.

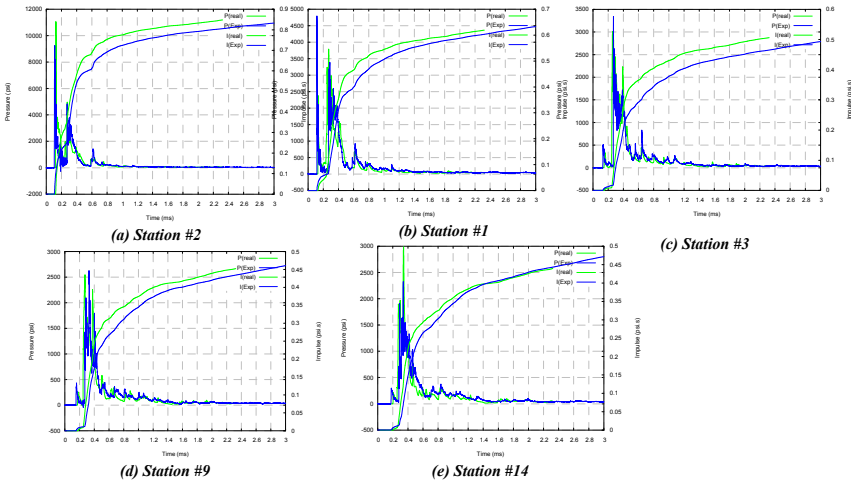


Figure 5: Comparison of measured and predicted pressure time histories at 5 locations along the center line.

3.3 Bare charges against deformable end plates

The bare cylindrical charges used in these tests are identical to those used above. Both are placed horizontally in the tube, with their center-of-gravity at the same



location. Both were tail-detonated. In this test sequence, the rigid, instrumented end wall is replaced by a set of deformable end plates (Fig. 6).

As the charges were identical, we used the previously computed flow fields at detonation completion, and interpolated them to the new domain. The flow field at detonation completion for the 174grams charge was interpolated onto the new CFD domain with deformable plates at $28\mu\text{s}$. The CFD domain is larger, as it also incorporates the domain upstream of the deformable end panels. The simulation was performed using the coupled CFD/CSD solver, where the CSD code is used to model the deformable end panels.



Figure 6: A bare charge placed in the tube against the deformable panels.

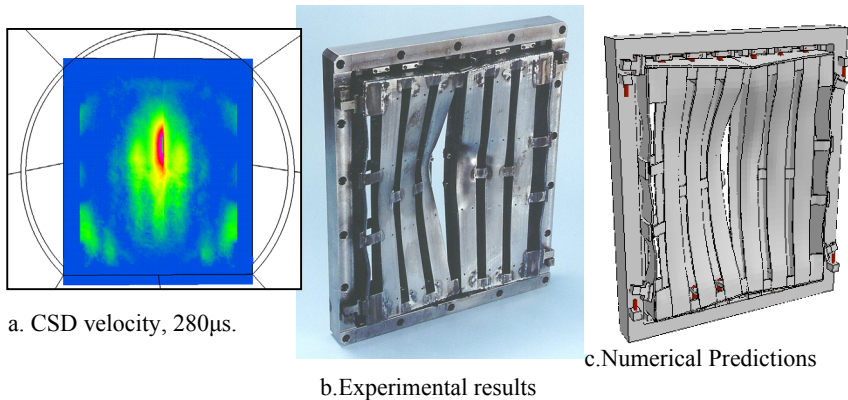


Figure 7: CSD velocity, $280\mu\text{s}$, and comparison of measured and predicted final deformations.

Figure 7a shows CSD velocity contours at $t=280\mu\text{s}$. This figure shows the maximum plate deflection and maximum CSD velocity value at jet impact location. The steel panels were only slightly damaged in response to this charge, with the larger deformation at the left leaf, immediately in front of the charge axis. The asymmetry in the deformable panel response to the charge resulted from structural differences between the leaves: the right leaf contains a large I-beam just behind the impact point, therefore strengthening locally the structure.

Comparison of measured and predicted panel velocities at three locations (two on the right leaf, one on the left leaf) shows good agreement in modeling the deformable panel response. The predicted maximum right leaf velocity is about 39m/s, reached at 0.47ms, compared to the experimental value of about 41m/s at 0.50ms. The predicted maximum left leaf velocity is 42.3m/s at 0.44ms, compared to the experimental value of about 40m/s at 0.46ms. Comparison of the measured (Fig. 7b) and predicted (Fig. 7c) final leaf deformations were in very good agreement, although the simulation predicted break-up of the right hinges, while the test results show that the hinges held.

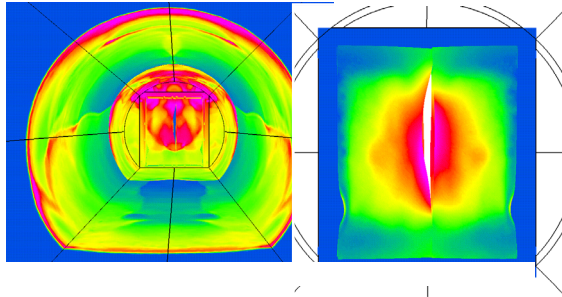


Figure 8: Pressure contours at 0.12 ms and CSD velocity contours at 0.45ms.

The second test against the deformable panels was conducted with the tail-detonated 263grams Composition-B charge. The flow field at the end of detonation was interpolated at 33.99 μ s onto the new extended domain with deformable plates. The coupled CFD/CSD solver was also used, the CSD handling the deformable leaves.

Analysis of the results shown in Fig 8a, at $t=0.12$ ms, shows the downstream propagating detonation wave, the multiple reflections of the incident wave from the deformable panels, the slight opening of the left leaf and the upstream propagating blast wave that came through the deforming leaves. Figure 8b shows CSD velocity contours on the leaves at 0.45ms, with a maximum velocity of about 100m/s at this time. Again, the left leaf is significantly more deformed.

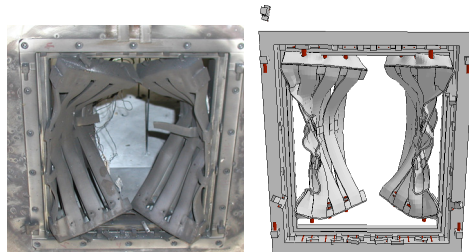


Figure 9: Comparison of measured and predicted panel deformation.

Figs. 9a and 9b shows a front view comparison of the measured and predicted panel deformation. The simulation was able to accurately predict most of the

structural deformation details. Certain aspects were not predicted as well: 1) The top and bottom latches were not as stout as built, and failed sooner than in the experiments; 2) The hinges broke much sooner, and resulted in larger deformation to the end plates than measures; and 3) Because of the previous two deficiencies, the panels were pushed in more than observed, and the extreme beams deformed more than observed. These discrepancies result from the fact that although the geometric details were modeled very accurately, these components were welded, and we lacked accurate data for the materials and welding process. In addition, hinge modeling is fairly tricky.

3.4 Computational resources

The 174grams charge detonation used a CFD mesh that contained about 38 million elements and 6.5 million nodes. The 263grams detonation simulation was conducted on a mesh of 53 million elements and 9.2 million nodes. Either of these flow fields was then interpolated onto a 75.2 million elements mesh (or 12.9 million nodes) for the rigid panel cases and onto a 103 million elements mesh (or 17.6 million nodes) for the deformable panels simulations. The deformable panels were modeled with 36,500 CSD shells. The complete detonation and coupled CFD/CSD simulation required about 4 to 5 days of computing on a 48-64 CPU's of SGI Origin 3900.

4 Conclusions and outlook

This paper described applications of a coupled CFD and CSD methodology to the simulation of blast waves generated by bare explosive charges in a test facility with rigid and deformable walls. The coupled algorithm that combined FEFLO98 (CFD) and MARS3D (CSD) was used with an embedded approach for which the CSD objects float through the CFD domain. This combination enables an easier and more accurate prediction of structural deformation, cracking and failure under blast loading.

Several experiments were conducted to characterize blast load and structural response as a function of charge size, ignition point (nose or tail) and orientation (horizontal or vertical). Very good agreements between the measured and predicted pressure and impulse time histories were obtained. The measurements and predictions identified the presence of a strong jet coming off the nose-end of the tail-end detonated charge. Stagnation of the jet on the end wall resulted in a large pressure and impulse amplitudes within a small circle on the cylinder axis line. The jet loading resulted in a minor damage to the deformable leaves for the smaller charge, and significantly more damage for the larger charge.

References

- [1] J.R. Cebal and R. Löhner - Conservative Load Transfer for Fluid-Structure-Thermal Simulations; Proc. 4th WCCM, Buenos Aires, Argentina, July (1998).



- [2] J.D. Baum, H. Luo and R. Löhner - The Numerical Simulation of Strongly Unsteady Flows With Hundreds of Moving Bodies; AIAA-98-0788 (1998).
- [3] J. D. Baum, et al., A Recent Developments of a Coupled CFD/CSD Methodology, AIAA 2001-2618, Proc.15th AIAA CFD Conf., CA (2001).
- [4] R. Löhner, Chi Yang, J. Cezbal, O. Soto, F. Camelli, J.D. Baum, H. Luo, E. Mestreau, D. Sharov, R. Ramamurti, W. Sandberg and Ch. Oh - Advances in FEFLO; AIAA-01-0592 (2001).
- [5] R. Löhner - Extensions and Improvements of the Advancing Front Grid Generation Technique; Comm. Num. Meth. Eng. 12, 683-702 (1996).
- [6] R. Löhner and J.D. Baum - Adaptive H-Refinement on 3-D Unstructured Grids for Transient Problems; Int. J. Num. Meth. Fluids 14, 1407-1419 (1992).
- [7] D. Pelessone and C.M. Charman - A General Formulation of a Contact Algorithm with Node/Face and Edge/Edge Contacts; 1998 ASME Pressure Vessels and Piping Conference, San Diego, Ca, July (1998).
- [8] R.G. Whirley and J.O. Hallquist - DYNA3D, A Nonlinear Explicit, Three-Dimensional Finite Element Code for Solid and Structural Mechanics - User Manual; UCRL-MA-107254 (1991), also Comp. Meth. Appl. Mech. Eng. 33, 725-757 (1982).
- [9] J.K. Gran – Experimental Characterization of a Scaled-Model general-Purpose Bomb, ISIEMS, 05-09 May 2003, Mannheim, GE.
- [10] M. Held – Blast Contour of Cylindrical Charges with Different Length to Diamete Ratios, ISIEMS, 05-09 May 2003, Mannheim, GE.

